A Bayesian approach to electric field and *E*-region neutral wind estimation with the Poker Flat Advanced Modular Incoherent Scatter Radar

Craig J. Heinselman[1] and Michael J. Nicolls[1]

[1]   In this paper, we describe an approach for computing vector electric fields in the *F* region and neutral winds in the *E* region from incoherent scatter radar (ISR) measurements, applicable especially for Advanced Modular Incoherent Scatter Radar (AMISR) systems, namely, the Poker Flat Incoherent Scatter Radar (PFISR). PFISR is a 128-panel (upgraded from 96 panels in September 2007) AMISR system installed at the Poker Flat Research Range near Fairbanks, Alaska. The pulse-to-pulse steering capabilities of AMISR support the measurement of line-of-sight velocities in multiple look directions essentially simultaneously. This capability in turn allows electric fields and neutral winds to be resolved with minimal assumptions regarding time stationarity of the medium. The multibeamforming capability also allows additional flexibility in the estimation of those parameters, for which experiment planning can become very important. The approach described herein is ideally suited for such planning, is appropriate for the overdetermined problem characteristic of AMISR measurements, and allows in a simple way for the inclusion of appropriate a priori information such as the assumption of negligible parallel electric fields and negligible vertical neutral winds. We present some case studies from the PFISR that demonstrate some of the new capabilities.

1. Introduction

[2] Advanced Modular Incoherent Scatter Radar (AMISR) technology opens up new avenues for experimental ionospheric research because of its unique steering and beam-forming capabilities. Electric field and vector velocity estimates are a critical product of AMISR operations. In most incoherent scatter (IS) experiments, there are significant limitations on the beam configuration that result in limited sampling of the velocity field. To obtain unambiguous ionospheric vector velocity estimates, the only method is to make three common volume measurements. With a single monostatic radar, this is of course not possible, and the only incoherent scatter radar (ISR) that can make such unambiguous measurements at the present time is the tristatic EISCAT UHF system [*Williams et al.*, 1984; *Schlegel and Moorcroft*, 1989]. Most radars thus resort to scanning, where the line-of-sight velocities are measured as the radar is steered in azimuth and elevation [e.g., *Doupnik et al.*, 1972; *Hagfors and Behnke*, 1974; *de la Beaujardière et al.*, 1977; *Wand and Evans*, 1981; *Sulzer et al.*, 2005]. Those line-of-sight velocities are then resolved into vector drifts in some coordinate system (typically a local approximation to the geomagnetic field) with the intrinsic assumption of time and spatial stationarity over the scan. There exist different methods of resolving the line-of-sight measurements that each contain their limitations and benefits. At high latitudes, the end goal is to produce estimates of the convection field as a function of magnetic latitude [e.g., *Horwitz et al.*, 1978; *Evans et al.*, 1979, 1980; *Banks et al.*, 1981; *Foster et al.*, 1981; *Holt et al.*, 1987; *Holt and van Eyken*, 2000].

[1]Center for Geospace Studies, SRI International, Menlo Park, California, USA.
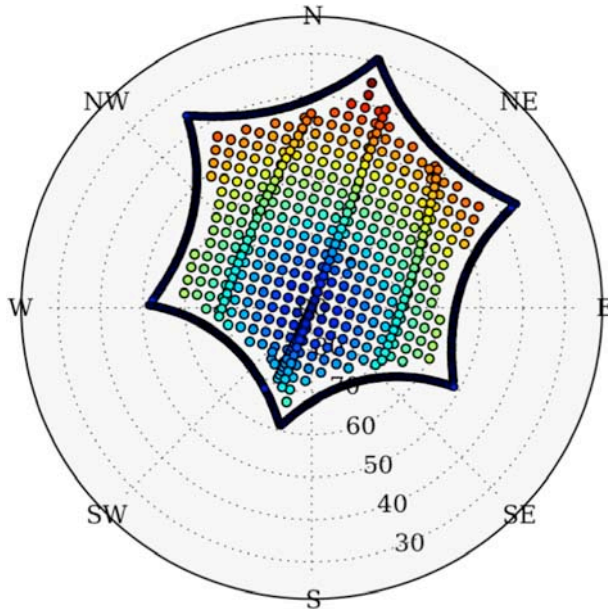
Figure 1. Possible look directions for the PFISR. The black star-shaped pattern indicates the grating lobe limits of the system.

[3] With AMISR technology, as we will discuss, the assumption of time stationarity over a duration of a scan is no longer needed, since "scanning" is not necessary. (We emphasize that time stationarity over an integration period is still necessary, an assumption intrinsic to IS spectral analysis.) Instead, with AMISR systems one forms multiple beams in the sky, steering on a pulse-to-pulse basis. This approach allows for the simultaneous measurement of plasma parameters in multiple look directions, since typically hundreds or thousands of pulses are integrated together. Fundamentally, this allows for the study of a class of problems untenable with scanning systems, where the velocity field changes rapidly during a scan time. Indeed, it is expected that a scanning system would produce velocity estimates that are inconsistent with any features of the true velocity field during the scan time if the velocity changes rapidly during the scan.

[4] In this paper we utilize this unique capability of AMISR systems to resolve velocities and electric fields. Our approach utilizes a scheme to combine the line-of-sight velocity estimates as a function of magnetic latitude. While different approaches are possible to retrieve vector velocities as a function of latitude from a set of line-of-sight velocities from beams spread in multiple look directions, we employ a method that combines a priori and measurement information to regularize the problem (qualitatively similar to a least squares approach

[e.g., *Holt et al.*, 1984]). This approach has other benefits, such as the ability to handle both the under- and overdetermined problems as well as being useful for experiment planning purposes. We use a similar approach to obtain wind vectors in the *E* region, which will allow for future investigations of Joule heating rates and neutral interactions. These first results demonstrate some of the unique capabilities of AMISR technology for upper atmospheric research.

2. The Poker Flat Incoherent Scatter Radar (PFISR)

[5] The Poker Flat Incoherent Scatter Radar (PFISR) is located at the Poker Flat Research Range (65.13°N, 147.47°W) near Fairbanks, Alaska. The radar has been running in normal user operations since March of 2007. PFISR underwent a system upgrade in September of 2007 to complete the "face", upgrading the number of panels from 96 to 128, which had the effect of increasing both aperture and transmit power (we estimate an increase in backscatter gain of approximately 33%, and in SNR of approximately 80%). AMISR technology allows the experimenter to steer the beam on a pulse-to-pulse basis using phased array techniques, providing a powerful extension over typical ISR approaches, which offer high-resolution measurements in one direction only, or reduced time resolution in multiple directions through physical steering. New avenues of research opened by this technology include IS spatial imaging [*Nicolls et al.*, 2007] and the ability to investigate problems with inherent time-space ambiguities, such as gravity wave propagation [*Nicolls and Heinselman*, 2007; *Vadas and Nicolls*, 2008].

[6] The radar itself is tilted so that its bore sight direction corresponds to an elevation angle of 74° and an azimuth angle (east of north) of 15°. This orientation was chosen to allow for as much downrange coverage as possible for the Poker Flat rocket corridors while also maintaining the ability to look up the local magnetic field line. Theoretically, any beam pointing configuration within the grating lobe limits is possible with AMISR systems. Practically, the PFISR consists of 473 preprogrammed look directions within the grating lobe limits. These positions, along with the grating lobe limits, are shown in Figure 1. The beamwidth of the system is approximately 1°, with the system gain decreasing proportional to the cosine of the angle off bore sight. More technical details of PFISR will be described in a future system description paper.

[7] The experimental configurations used in the case studies presented in this paper are general purpose setups designed in particular for electric field measurements. Beam configurations are shown for two setups in Figure 2 where the elevation and azimuth angles of the beam
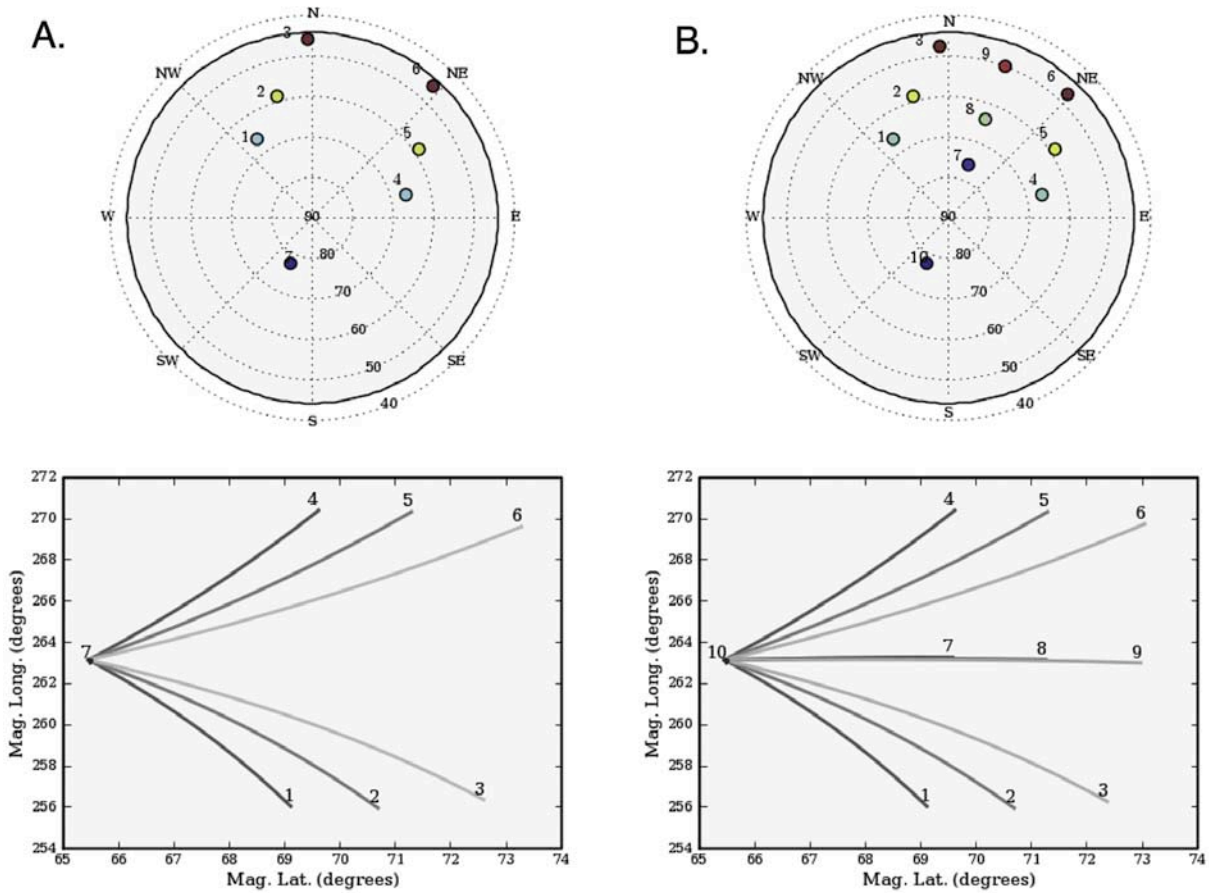
Figure 2. Experimental configuration for two PFISR modes, (A) a seven-beam mode and (B) a 10-beam mode. The top plots shows the azimuth and elevation for the beams, and the lower plots shows the magnetic latitude versus longitude coverage of the beams with the lines extending from 0 to 1000 km. Beam 7 and 10 of experiments A and B, respectively, point up the geomagnetic field line.

positions are shown in addition to the look patterns as a function of magnetic latitude and longitude, with the lines representing the range of observation (out to 1000 km). The first mode (Figure 2A) employs seven beam positions, including three pairs of beams spread in magnetic latitude and one beam pointed up the magnetic field line. The seven beam positions (labeled for identification) are spread in magnetic latitude for determination of the electric field structure as a function of latitude. The second mode (Figure 2B) consists of an additional 3 beams along the magnetic meridian, and the farthest downrange set of beams has a slightly higher elevation angle. In geographic coordinates, the beams end up being spread in the east and the west and look toward the north, with the up-**B** position (labeled 7 and 10 in Figures 2A and 2B, respectively) pointed slightly to the south. The dip angle will of course vary from beam to beam, but is

in the range of $75°–85°$ in the *F* region. Beam pairs (1–4, 2–5, 3–6 in Figure 2A) or triplets (1–4–7, 2–5–8, 3–6–9 in Figure 2B) have approximately the same elevation angles with the third pair/triplet pointed farthest downrange.

[8] The transmission schemes for these experiments consisted of an interleaving of long pulses (480 μs, corresponding to ~72 km of range smearing) for *F* region measurements and 30 μs (4.5 km) alternating code pulses [*Lehtinen and Häggström*, 1987] for *E*-region measurements. The fully functional PFISR system has a transmit power of about 16 kW per panel (about 1.5 MW for the 96-panel system and 2.0 MW for the 128-panel system). True transmit power is closer to 1.3 MW and 1.7 MW for the 96 and 128 panel systems, respectively, with the difference due to nonoperational

solid state power amplifiers. PFISR has a maximum duty cycle of about 10%.

[9] A major advantage of AMISR systems over traditional ISRs is that no scanning is necessary. That is, the time resolution of vector velocity estimates is not limited by the physical movement time of the antenna; instead, the time resolution is limited by the ionospheric conditions, the sensitivity of the system, and the statistical nature of the IS measurements. Nevertheless, assumptions regarding the spatial homogeneity of the velocity field must still be made. In many cases, including in the experiment described here, the goal is to measure the velocity field as a function of magnetic latitude. This approach is accomplished by forming beams that provide significant magnetic latitude coverage so that a solution can be obtained with minimal covariance between the resolved velocity components while at the same time minimizing the assumptions regarding spatial homogeneity.

3. Velocity Estimation

3.1. Line-of-Sight Velocities

[10] There are several "classical" ways of estimating line-of-sight (LOS) velocities from the incoherent scatter spectrum. Fundamentally, the LOS velocity corresponds to the Doppler shift of the spectrum, and a spectral moment method or a fit to the phase angle both work equally well. However, for asymmetric (noisy) spectra these methods may introduce biases. In our analysis, we estimate LOS velocities from a fit to the full incoherent scatter autocorrelation function (including both the real and imaginary parts). Errors on the fit are estimated using the estimated Jacobian at the values of the estimated parameters. Once LOS drifts are obtained, vector drifts must be estimated using multiple spaced beams.

3.2. Vector Velocities

[11] The application of ionospheric velocity measurements involves resolving those measurements into some coordinate system. Any LOS velocity measurement i can be written in terms of the component in some coordinate system defined by the unit vector $\mathbf{k} = [k_x \ k_y \ k_z]^T$,

$$v_{los}^i = k_x^i v_x + k_y^i v_y + k_z^i v_z. \tag{1}$$

[12] In the case of a radar-centered geographic coordinate system, the appropriate $\mathbf{k}$ vector to use is defined in terms of the direction cosines to the observation volume,

$$\mathbf{k} = \begin{bmatrix} k_e \\ k_n \\ k_z \end{bmatrix} = \begin{bmatrix} \cos\alpha \\ \cos\beta \\ \cos\gamma \end{bmatrix} = \begin{bmatrix} x \\ y \\ z \end{bmatrix} R^{-1} \tag{2}$$

where subscripts e, n, and z refer to east, north, and up, respectively; x, y, and z correspond to zonal, meridional, and vertical geodetic distance to the observation volume in a radar-centered cartesian coordinate system; and $R = \sqrt{x^2 + y^2 + z^2}$ is the range. For high elevation angles, negligible Earth curvature effects can be assumed, in which case the radar $\mathbf{k}$ vector is simply

$$\mathbf{k} = \begin{bmatrix} k_e \\ k_n \\ k_z \end{bmatrix} = \begin{bmatrix} \cos\theta \ \sin\phi \\ \cos\theta \ \cos\phi \\ \sin\theta \end{bmatrix} \tag{3}$$

where θ is the elevation angle and ϕ is the azimuth angle (east of north) of the particular look direction.

[13] In the case of a local geomagnetic coordinate system, we can then use the rotation matrix

$$R_{geo \rightarrow gmag} = \begin{bmatrix} \cos\delta & -\sin\delta & 0 \\ \sin I \sin\delta & \cos\delta \sin I & \cos I \\ -\cos I \sin\delta & -\cos I \cos\delta & \sin I \end{bmatrix} \tag{4}$$

where δ (about $22°$ for the PFISR site location) is the declination angle and I is the dip angle (about $77.5°$ for the PFISR site location) for the observation volume, which leads to

$$\mathbf{k} = \begin{bmatrix} k_{pe} \\ k_{pn} \\ k_{ap} \end{bmatrix} = \begin{bmatrix} k_e \cos\delta - k_n \sin\delta \\ k_z \cos I + \sin I (k_n \cos\delta + k_e \sin\delta) \\ k_z \sin I - \cos I (k_n \cos\delta + k_e \sin\delta) \end{bmatrix}. \tag{5}$$

where subscripts pe, pn, and ap refer to perpendicular east, perpendicular north, and antiparallel, respectively. These equations use reasonable local approximations to the magnetic field; however, a more exact method would be to define a geomagnetic coordinate system (e.g., with respect to the magnetic apex [*VanZandt et al.*, 1972; *Richmond*, 1995]) and rotate the direction cosine $\mathbf{k}$ vector to that system.

[14] A standard method for estimating perpendicular velocities and electric fields at high latitudes uses two measurements and the assumption of identically zero parallel velocity to produce an estimate of the two perpendicular components [e.g., *de la Beaujardière et al.*, 1977]. In this case, the two measurements correspond to

$$\begin{bmatrix} v_{los}^1 \\ v_{los}^2 \end{bmatrix} = \begin{bmatrix} k_{pe}^1 & k_{pn}^1 & k_{ap}^1 \\ k_{pe}^2 & k_{pn}^2 & k_{ap}^2 \end{bmatrix} \begin{bmatrix} v_{pe} \\ v_{pn} \\ v_{ap} \end{bmatrix}. \tag{6}$$

These two measurements can then be used to solve the algebraic equations for v_{pn} and v_{pe}. For example, one obtains for v_{pn}:

$$
v_{pn} = \frac{v_{los}^1 - \dfrac{k_{pe}^1}{k_{pe}^2} v_{los}^2 - v_{ap}\left(k_{ap}^1 - k_{ap}^2 \dfrac{k_{pe}^1}{k_{pe}^2}\right)}{k_{pn}^1\left(1 - \dfrac{k_{pn}^2 k_{pe}^1}{k_{pn}^1 k_{pe}^2}\right)}
$$

$$
\approx \frac{v_{los}^1 - \dfrac{k_{pe}^1}{k_{pe}^2} v_{los}^2}{k_{pn}^1\left(1 - \dfrac{k_{pn}^2 k_{pe}^1}{k_{pn}^1 k_{pe}^2}\right)} \tag{7}
$$

where the simplification ignores the parallel component of the drift, often a good assumption at high latitudes where the dip angle is large and the drifts are dominated by horizontal motion. This equation indicates that the **k** vector components in at least one of the principal directions must be significantly different for the individual measurements. Otherwise, the denominator of equation 7 tends to 0. This can be more readily seen by propagating the errors for the v_{pn} estimate, in doing so finding that the variance of v_{pn} becomes,

$$
\sigma_{v_{pn}}^2 = \frac{\sigma_{v_{los}^1}^2 + \sigma_{v_{los}^2}^2\left(\dfrac{k_{pe}^1}{k_{pe}^2}\right)^2}{\left[k_{pn}^1\left(1 - \dfrac{k_{pn}^2 k_{pe}^1}{k_{pn}^1 k_{pe}^2}\right)\right]^2} \tag{8}
$$

These results indicate that the radar must be either steered or multiple beams used to resolve the velocity components, an intuitive conclusion.

[15] In this approach, each estimate is unique and unambiguous although all available information is clearly not used (the method is not optimal, in any sense) and the covariance of the estimates will depend on the geometry of the experiment (in most cases with high-latitude radars, the scanning geometry). The approach cannot handle additional measurements since additional information will make the solution overdetermined and, under the worst conditions, yield no solution. For AMISR systems, the "two-point" estimates could be binned in magnetic latitude (averaged after the fact) to produce electric field estimates as a function of latitude. However, this approach is not desirable for AMISR operations since it can neither handle an arbitrary number of beams nor arbitrary pointing geometry. For example, the approach would work for the pairs of beams in Figure 2A, but not for the triplets of beams in Figure 2 since the problem has become overdetermined with the additional beams along the meridian. It would then become unclear how to combine the estimates if one wishes to produce vector drifts as a function of magnetic latitude.

[16] Thus we employ a more optimal approach that combines all samples within a particular magnetic latitude bin to produce a single estimate with a full error covariance estimate. This approach is more optimal in combining multiple line-of-sight velocity measurements and can handle the overdetermined problem.

[17] Given that the velocity field is spatially uniform, the Bayesian linear model for a particular measurement can be written as

$$
v_{los}^i = \mathbf{k}^i \cdot \mathbf{v}_i + e_{los}^i. \tag{9}
$$

That is, each measurement represents a sample of the vector field (dot product of the geometry vector with the velocity field) plus an error associated with the line-of-sight velocity estimate (which comes directly from the nonlinear least squares fitting procedure described previously). Multiple measurements can be written in matrix form

$$
\begin{bmatrix} v_{los}^1 \\ v_{los}^2 \\ \vdots \\ v_{los}^n \end{bmatrix} = \begin{bmatrix} k_{pe}^1 & k_{pn}^1 & k_{ap}^1 \\ k_{pe}^2 & k_{pn}^2 & k_{ap}^2 \\ \vdots & \vdots & \vdots \\ k_{pe}^n & k_{pn}^n & k_{ap}^n \end{bmatrix} \begin{bmatrix} v_{pe} \\ v_{pn} \\ v_{ap} \end{bmatrix} + \begin{bmatrix} e_{los}^1 \\ e_{los}^2 \\ \vdots \\ e_{los}^n \end{bmatrix} \tag{10}
$$

or

$$
\mathbf{v}_{los} = A\mathbf{v}_i + \mathbf{e}_{los}. \tag{11}
$$

If we treat $\mathbf{v}_i$ as a Gaussian random variable (hence, the Bayesian model), the realization of which we wish to estimate, we can use linear theory to derive a least squares estimator. For our case, we take $\mathbf{v}_i$ to be zero mean and with covariance Σ_v. This covariance matrix then includes the a priori information to be imposed on the data—the expected range of variability of the velocity in different directions. We also take the measurement error vector to be Gaussian, zero mean, and with covariance Σ_e. Given these constraints, one can show that the least squares estimator is the affine function (actually, a linear function for this zero-mean case) [e.g., *Aster et al.*, 2005; *Tarantola*, 2005]

$$
\hat{\mathbf{v}}_i = \Sigma_v A^T \left(A\Sigma_v A^T + \Sigma_e\right)^{-1} \mathbf{v}_{los}. \tag{12}
$$

The covariance of the estimate is given by

$$
\Sigma_{\hat{v}} = \Sigma_v - \Sigma_v A^T \left(A\Sigma_v A^T + \Sigma_e\right)^{-1} A\Sigma_v
$$
$$
= \left(A^T \Sigma_e^{-1} A + \Sigma_v^{-1}\right)^{-1} \tag{13}
$$

The second expression for the covariance matrix shows how new information from the measurements (with

covariances Σ_e) reduces the covariance of the estimate. The effectiveness of the new information is determined by the geometry information in A.

[18] This formulation has a number of very desirable properties for generalized processing. Probably the most important is that it properly accounts for the measurement variances (via Σ_e) for any number of line-of-sight velocity measurements. In fact, it favors using more than three line of sights as the additional information is weighted accordingly. On the other hand, it also supports as few as one measurement with the additional components determined from the a priori estimates (taken to be 0). This could potentially cloud this lack of data except that the variance estimates will be driven by the relatively large Σ_v variances in the directions not supported by the measurements. This method would thus work equally well with multiple position data from scans or with position pairs, without requiring a change in algorithm.

[19] The goal of the velocity measurements is essentially to produce an estimate of the vector velocities from measurements of the line-of-sight velocities within a particular magnetic latitude bin. Doing this estimation in bins of magnetic latitude allows us to resolve the vector velocities as a function of latitude. While one approach (perhaps the most obvious) is to use two-point measurements and then average in magnetic latitude, the approach described here more optimally uses the full covariance of the measurements. A more rigorous comparison of different approaches will be investigated and compared in future work, including the possibility of using regularization information (similar to the method described by *Sulzer et al.* [2005]) as a function of latitude or using different types of priors (such as entropy [e.g., *Hysell*, 2007]).

[20] As a validation of PFISR measurements of vector drifts, in Figure 3 we compare the measured vector velocities on 19 January 2007 to measurements onboard two instrumented rockets that were launched as part of the JOULE 2 campaign [e.g., *Hysell et al.*, 2008]. The PFISR data were collected in the 7-beam measurement scheme of Figure 2A and processed at 1-minute time resolution with overlapping bins in magnetic latitude for ease of comparison. The right of Figures 3A and 3B shows the vectors measured by PFISR near the time of the launches (1229 UT and 1245 UT in Figures 3A and 3B, respectively) as a function of time and magnetic latitude. Predominant eastward flows with maximum values greater than 1000 m/s can be seen during the first launch. During the second launch, flows were much smaller and more uniform with latitude.

[21] The electric field data gathered on the rocket were measured using the double probe technique [e.g., *Pfaff*, 1996] in which a pair of crossed dipoles provided vector measurements of the DC electric field in the plane perpendicular to the ambient magnetic field. The component of the electric field in the direction of the magnetic field was not measured and was assumed to be zero at these altitudes. The electric field data are converted to $\mathbf{E} \times \mathbf{B}$ velocities using a magnetic field model and are displayed in Figure 3 along the trajectory of the rocket for the times shown. The first instrumented rocket was launched at 1229 UT and followed a predominantly northward direction, achieving an apogee of 190 km at 229 seconds after lift off. The second rocket was launched at 1245 UT and achieved an apogee of 217 km at 235 seconds after lift off. Data are shown for both the upleg and downleg portions of the flight, for the time period when the payload was at altitudes greater than approximately 100 km. This corresponded to about 260 seconds of flight time, as shown in Figure 3 [R. F. Pfaff, personal communication, 2008].

[22] The rocket trajectory was mapped to the PFISR field of view. The rocket-measured flow vectors are plotted in black along the trajectory in Figure 3. In the first launch, qualitative agreement can be seen: small drifts (few hundred m/s) up to $\sim66.3°$ a large enhancement in the convection above this level within a narrow latitudinal channel, and a decrease to negligible values at higher latitudes. In the second launch, the vectors appear quite uniform by comparison, with a steady drift of $\sim300-400$ m/s and a decrease at higher magnetic latitudes. The left of Figures 3A and 3B show more quantitative comparisons, where we have plotted the rocket meridional and zonal drifts in blue as a function of magnetic latitude along with the PFISR drifts in the time and latitude bin closest to the rocket trajectory. During the first launch, the PFISR measurements are able to reproduce the enhancement in convection at $\sim66.5°$ and the decrease at higher latitudes, although at higher latitudes the PFISR measurements become noisy, both because of the higher ranges that these measurements correspond to and because of the small drift magnitude, which causes some of the assumptions to break down. During the second launch, the zonal flow is well represented. The rocket-measured meridional flow is quite small (never greater than 100 m/s, and fluctuating about 0 at the lower latitudes). The PFISR measurements show good agreement at the lower latitudes but begin to diverge, likely as a result of a breakdown in one of the assumptions: either a violation of L-shell uniformity or an increased contribution from the parallel flows resulting from the small $\mathbf{E} \times \mathbf{B}$ drift magnitude. Overall, the comparison with the rocket is quite favorable and illustrates the ability of PFISR to resolve spatial (latitudinal) and temporal features of the electric fields.

3.3. Experiment Planning

[23] The approach described above to combine LOS velocities can also be used for an efficient means of experiment planning. Because of the flexibility of the
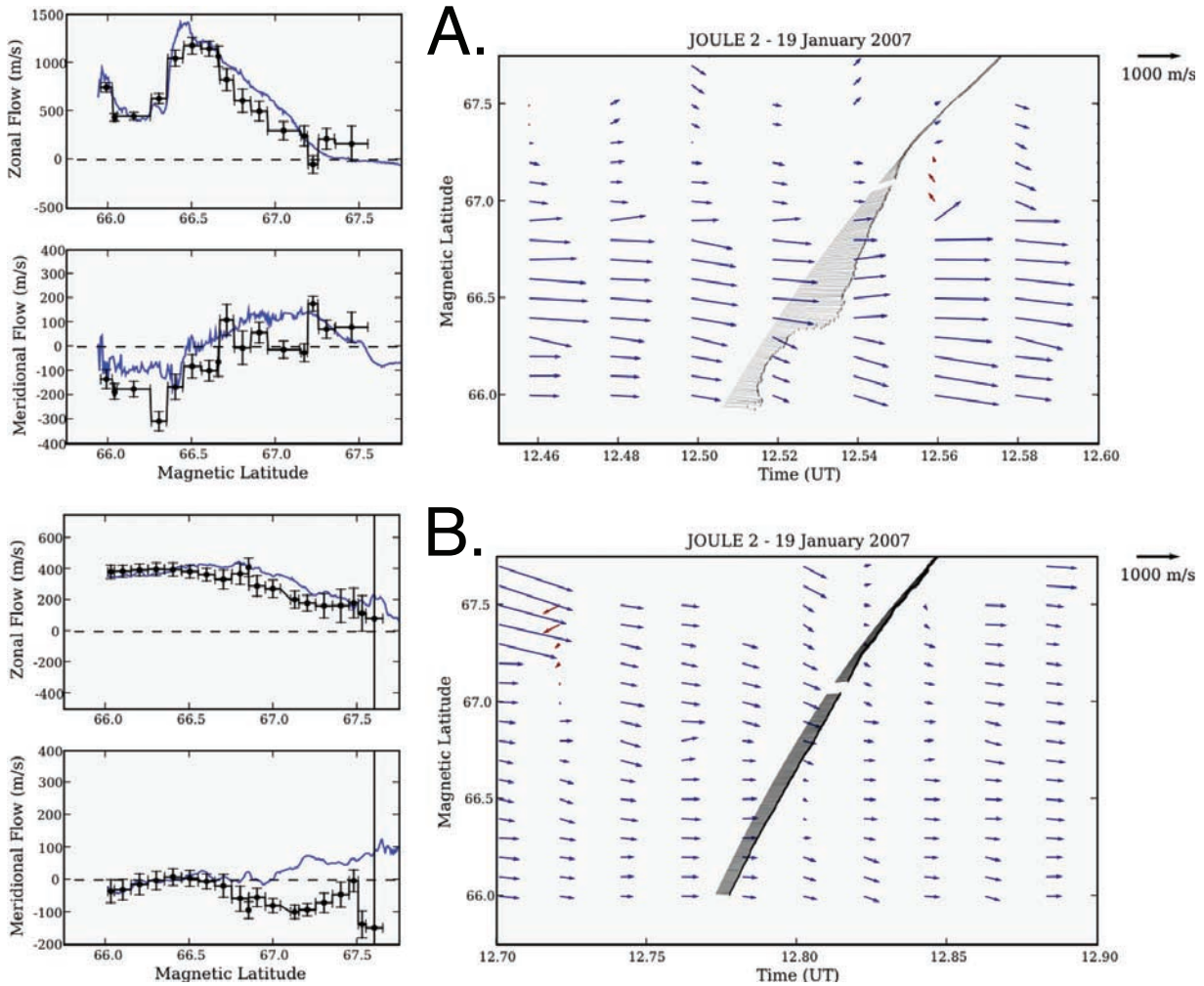
Figure 3. Comparison between PFISR-derived vector drifts using the assumptions and techniques described in the paper with vector drifts derived from rocket-measured electric fields. (left) The panels show the zonal and meridional flow comparisons (rocket in blue, PFISR in black, with errorbars). (right) The panels shows a quiver plot of the drifts, with the rocket trajectory and drifts overplotted. (A) corresponds to the first launch (1229 UT), and (B) corresponds to the second launch (1245 UT).

pointing geometry of AMISR systems, choosing suitable beams to achieve a given scientific goal is important. Because equation 13, the a posteriori covariance in model space, does not depend on the absolute LOS velocities, but only on the a priori covariance, error covariance (assumed to be diagonal), and geometry matrix, the standard error and covariance of a given experimental setup can be evaluated for planning purposes. As an example, we compare the predicted variances and covariances of the two setups in Figure 2, as well as the case where we use only half the beams in the 10-beam setup (these are referred to below as cases 1, 2,

and 3 respectively). The latter approach might be useful if one wishes to produce vector velocity estimates as a function of latitude along two meridians, for example to examine the homogeneity of the zonal flow.

[24] In Figure 4, we show the results of the comparison. Here we show the standard errors (Figure 4, top) and error ellipses (Figure 4, bottom) for the three cases. We have attempted to replicate as closely as possible the real geophysical case. We have assumed that each of the beams samples the LOS velocity every 35 km ($\sim$ half the pulse width) and have used a latitudinal binning of $0.5°$. We have used data only from altitudes 150 km or higher
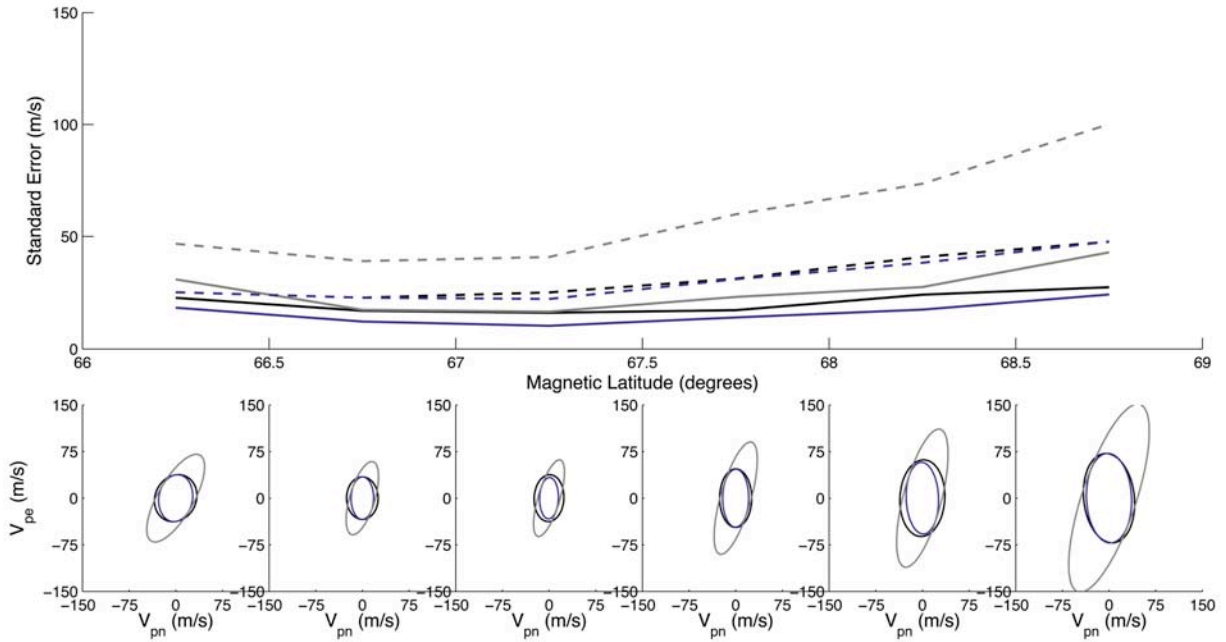
Figure 4. Comparison of standard errors and error ellipses for three experiments: Figure 2A (black), Figure 2B (blue), and one half of Figure 2b (gray). (top) The panel shows the standard error for the zonal (dashed) and meridional (solid) directions. (bottom) The panel shows the 1-σ error ellipses as a function of magnetic latitude. Half-degree magnetic latitude spacing is used; see text for more details.

(where the plasma can be assumed to be collisionless). For the error covariance matrix, we have assumed that the LOS velocity variances are proportional to range squared and chosen an arbitrary scaling constant of 10 m/s errors at 100 km. Σ_e is also assumed to be diagonal. For the a priori matrix, Σ_v, we have assumed diagonality and chosen standard errors of 3000 m/s for the perpendicular directions and 15 m/s for the parallel direction. The parallel number was chosen by examining the statistics of a long duration data set of up-**B** measurements.

[25] From Figure 4, it is clear that the zonal errors are always larger than the meridional errors. This is a geometrical effect caused by the proximity of the beams in azimuth. The errors increase as a function of range because of the assumed range dependence of the LOS errors. The errors are slightly larger in the first latitudinal bin because only one pair/triplet of beams satisfies the altitudinal condition stated above, so that there are fewer samples within that bin. Comparing case 1 and case 2 curves (black and blue, respectively) one sees that adding the beams in the meridian decreases the errors in the meridional component, as one would expect. The zonal estimate is only slightly improved. For case 3, where we have dropped out 3 of the beams from case 2, one sees a

large increase in the zonal errors and a smaller increase in the meridional errors.

[26] Looking at the error ellipses, the ellipsoidal but unskewed shape of the case 2 and 3 curves is representative of a well-chosen set of look directions. The case 2 curves are slightly narrower in the meridonal direction because of the additional meridional beams. For case 3, there is significant correlation between the two errors. The tradeoff between using a setup like case 1 versus case 2 becomes the increased precision versus time resolution (which of course will increase as more beams are used). Additionally, by using a scheme like that of case 2, one can produce two noisier (and correlated) estimates along two separate meridians.

3.4. E-Region Winds

[27] A second application of the approach described in section 3.2 is to the measurement of E-region winds. At any given altitude, the ions will approximately satisfy a simplified steady state ion momentum equation neglecting gravity and diffusion (but including winds and electric fields) [e.g., *Kelley*, 1989],

$$0 = e(\mathbf{E} + \mathbf{v}_i \times \mathbf{B}) - m_i \nu_{in}(\mathbf{v}_i - \mathbf{u}) \qquad (14)$$

where e is the charge on an electron, $\mathbf{E}$ is the electric field, $\mathbf{v}_i$ is the ion velocity, $\mathbf{B}$ is the magnetic field, m_i is the ion mass, v_{in} is the ion-neutral collision frequency, and $\mathbf{u}$ is the neutral wind vector. Defining the matrix C as

$$C = \begin{bmatrix} \left(1 + \kappa_i^2\right)^{-1} & -\kappa_i\left(1 + \kappa_i^2\right)^{-1} & 0 \\ \kappa_i\left(1 + \kappa_i^2\right)^{-1} & \left(1 + \kappa_i^2\right)^{-1} & 0 \\ 0 & 0 & 1 \end{bmatrix} \quad (15)$$

where $\kappa_i = e\, B/m_i v_{in} = \Omega_i/v_{in}$ is the ratio of gyrofrequency to collision frequency, the ion velocity can be solved for in geomagnetic coordinates as

$$\mathbf{v}_i = b_i C \mathbf{E} + C\mathbf{u} \quad (16)$$

where $b_i = e/m_i\, v_{in} = \kappa_i/B$ is the ion mobility. Defining a new matrix $D = [b_i\, C\ C]$ then the Bayesian linear model becomes

$$\mathbf{v}_{los} = (A \cdot D)\mathbf{x} + \mathbf{e}_{los} \quad (17)$$

where A is still the matrix defining the geometrical mapping from orthogonal velocity components to the beam's line of sight.

[28] There is an obvious problem with this model in that it is ambiguous in terms of the components of $\mathbf{E}$ and $\mathbf{u}$. The solution is to use an altitude profile of measurements which have different D matrices for different altitudes. The electric field can be assumed to map along the field lines but the neutral wind must be allowed to vary with altitude. This general technique has been used for many years to estimate neutral winds in the E region [e.g., *Fedde and Banksr*, 1972; *Brekke and Doupnik*, 1973]. This assumption can be simply incorporated by adding neutral wind velocities for a set of altitudes to the forward model vector, $\mathbf{x} = [E_{pe}\ E_{pn}\ E_{\parallel}\ u_{pe}^1\ u_{pn}^1\ u_{\parallel}^1\ u_{pe}^2\ u_{pn}^2\ u_{\parallel}^2 ... u_{pe}^n\ u_{pn}^n\ u_{\parallel}^n]^T$. For the electric field and neutral wind information to become decoupled, we must use some measurements at altitudes where the neutral wind component is negligible. In other words, we utilize both F region long pulse velocity measurements (which contain only contributions from the electric field) and alternating code E-region measurements in the forward model. This approach produces a full set of neutral wind vectors as a function of altitude. We should point out that in general the meridional neutral winds will be better determined than the zonal winds if a look direction up the magnetic field line is used in the inversion scheme, since the meridional winds will dominate that motion (diffusion is neglected). In addition, it is important to realize that the results of this approach are sensitive to the collision frequency, which must in general be obtained from a neutral atmospheric model like MSIS [*Hedin*, 1991].

[29] The a priori covariance matrix, Σ_v, requires a little bit of care in this formulation. Since we have cast the problem into a coordinate system appropriate for the electric fields (a local approximation to the geomagnetic field), the covariance of the wind estimates is not obvious. One constraint that should be applied is the assumption that the vertical wind is small or negligible. This can be accomplished by formulating Σ_v^{geo} in geographic coordinates, and rotating it to geomagnetic, which will introduce off diagonal terms into Σ_v^{gmag}. The rotation is done using a straightforward transformation,

$$\Sigma_v^{gmag} = J_{geo \to gmag} \Sigma_v^{geo} J_{geo \to gmag}^T \quad (18)$$

where $J_{geo-gmag}$ is the Jacobian matrix appropriate for the rotation. Practically, this matrix contains copies of $R_{geo \to gmag}$ along its diagonal.

[30] Note that the inversion is done in the local geomagnetic coordinate system; then, the wind vectors can be transformed to geographic coordinates using the transformation matrix

$$R_{gmag \to geo} = \begin{bmatrix} \cos\delta & \sin I \sin\delta & -\cos I \sin\delta \\ -\sin\delta & \cos\delta \sin I & -\cos I \cos\delta \\ 0 & \cos I & \sin I \end{bmatrix}. \quad (19)$$

[31] The a posteriori covariance matrix can also be rotated to geographic coordinates using an analogous expression to equation 18. A comparison of our approach to that of more traditional methods [e.g., *Azeem and Johnson*, 1997; *Johnson et al.*, 1987; *Johnson*, 1990; *Johnson and Virdi*, 1991] will be investigated in future work. The combination of electric fields and E-region neutral winds using the approaches described here can then be used to compute additional products, such as height-resolved Joule heating rates [e.g., *Thayer*, 1998, 2000].

4. Results

[32] In this paper, we focus on the results of one night of observations, 13 February 2007, which exhibited a moderate degree of auroral activity. These data were taken in the 7-beam mode in Figure 2A. Figure 5A show the raw electron densities with no correction for T_e/T_i or Debye length effects. The alternating code data (4.5-km range resolution) have been plotted up to 150 km, and above this level the oversampled long pulse (72-km range resolution with 4.5-km sampling) has been used. Most of the activity on this night occurred after about 0930 UT (UT = LST + 9 hours), when steady, moderately energetic, precipitation caused a fairly steady band of ionization centered at about 110 km. This precipitation was accompanied by softer particles at higher altitudes, which is important for accurately determining the line-of-sight drifts in the F region and subsequently the
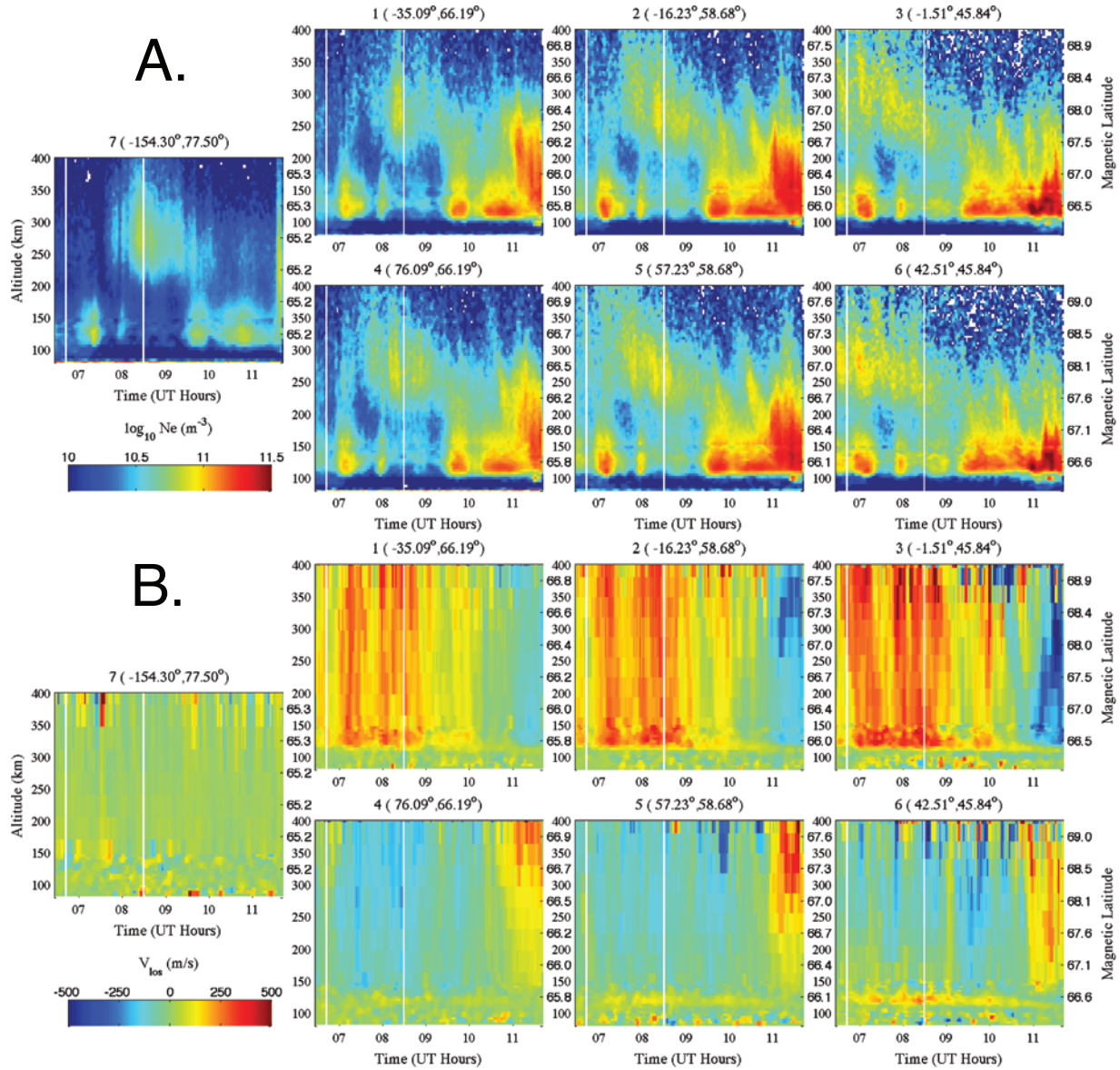
Figure 5. (A) Raw electron densities and (B) line-of-sight ion velocities for the seven beam positions from the alternating code (up to 150 km) and long pulse (above 150 km) measurements on 13 February 2007. Altitude is indicated on the left *y* ordinate and magnetic latitude is indicated on the right *y* ordinate.

electric fields. After about 1100 UT, a broader spectrum of precipitation caused an increase in ionization below 100 km and up to about 250 km. The auroral ionization was observed in all beams, however it is clearly strongest toward the north (downrange beams) and weakest in the beam pointed up the magnetic field line (recall that this beam is pointed slightly to the south, see Figure 2). Looking at the line-of-sight ion drifts, which are plotted

in Figure 5B the clear anticorrelation between the westward- and eastward-looking beams imply dominant zonal motion. The strongest line-of-sight drifts are observed in the downrange beams and are in excess of 500 m/s. A large-scale reversal occurs close to 11 UT. The drifts are in general larger in the westward-looking beams implying some small northward meridional flow prior to reversal and some small southward meridional
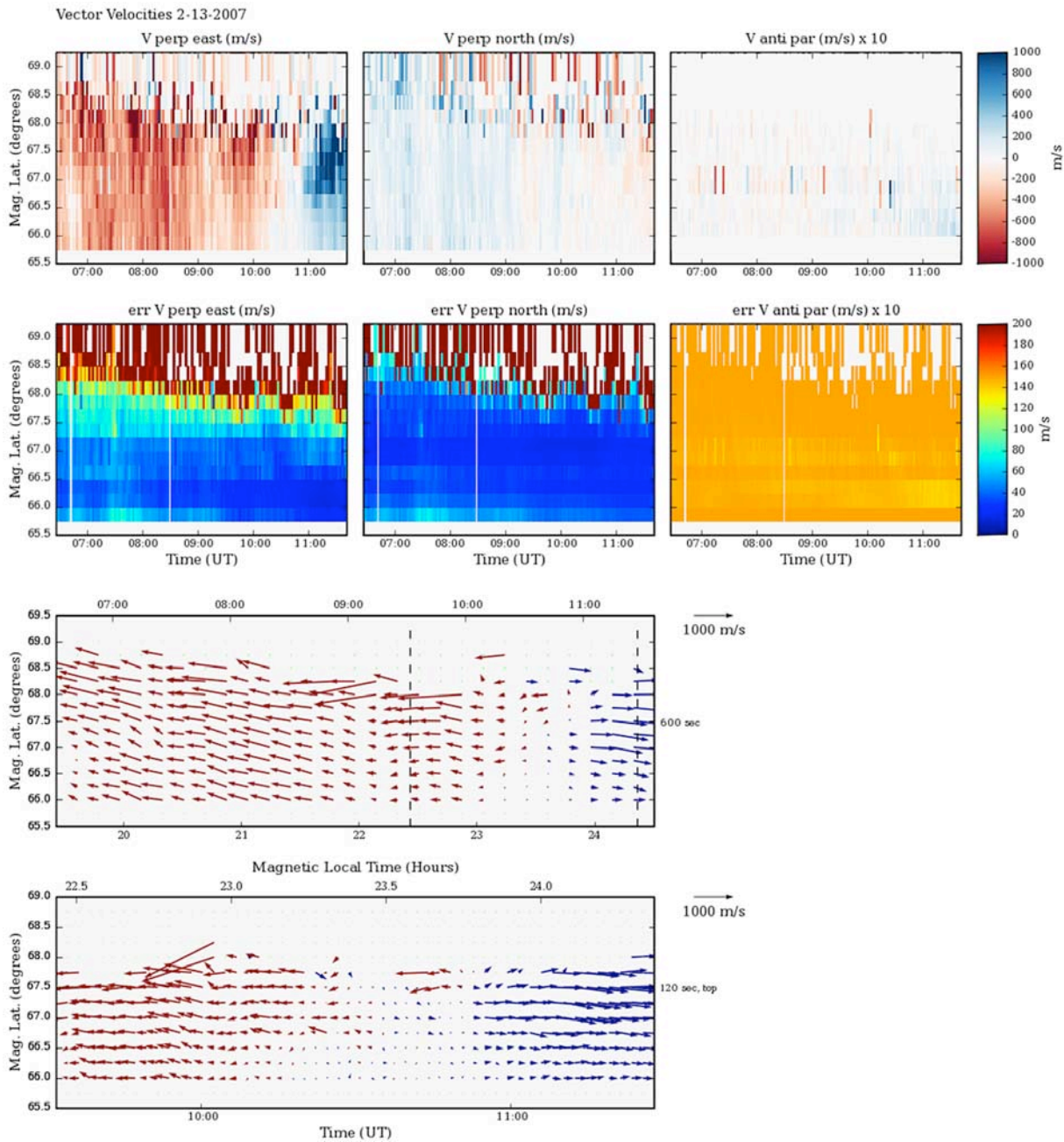
Figure 6. Vector velocity estimates on the night of 13–14 February 2007. (top) The panels show the perpendicular east, perpendicular north, and antiparallel velocities along with error estimates as a function of time and magnetic latitude. The top quiver plot shows the vector velocity estimates with arrows (blue indicating eastward drifts and red indicated westward) at 10-minute resolution. The lower quiver plot shows the zoomed-in region indicated by the dashed vertical lines at 2-minute resolution.
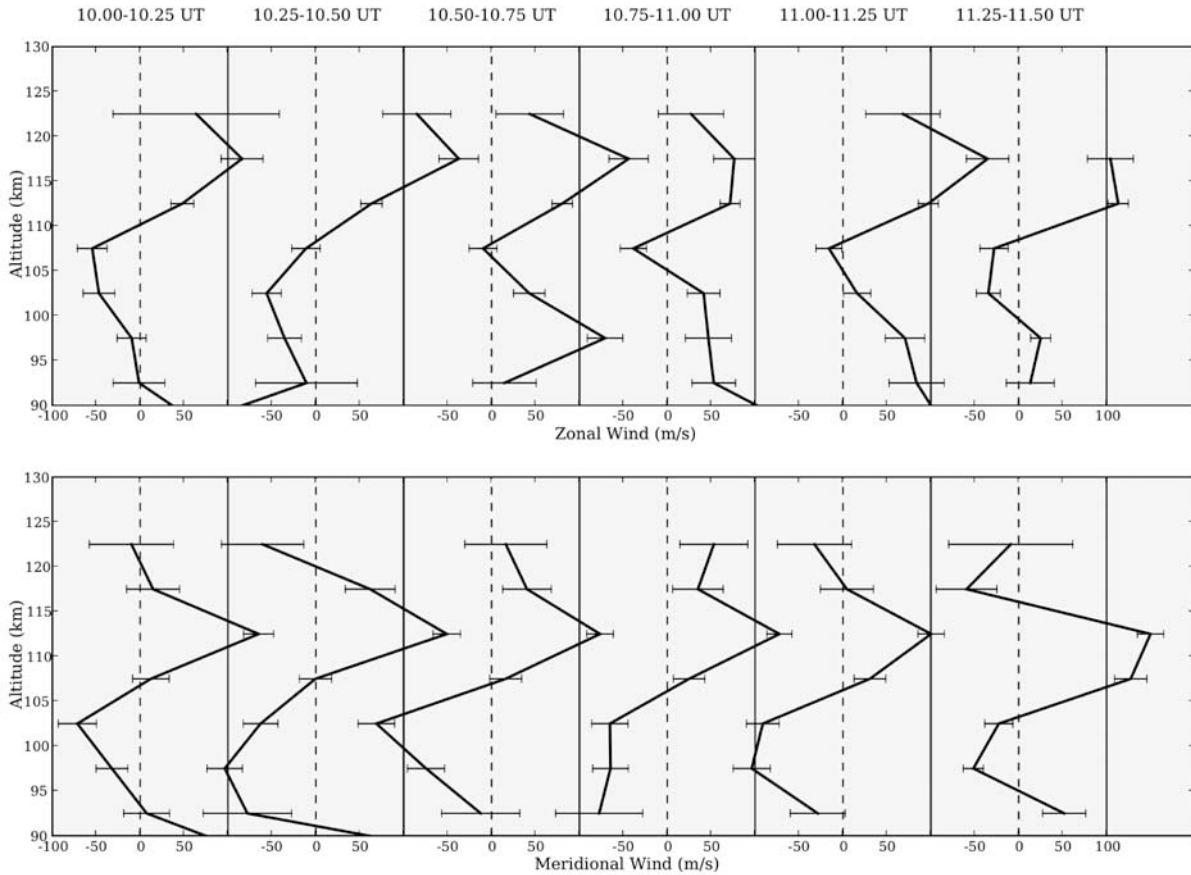
Figure 7. (top) Zonal and (bottom) meridional *E*-region wind profiles in 15-minute time bins for the night of 13 February 2007.

flow after reversal. We emphasize the altitude variation of the drifts. In the *F* region and upper *E* region (above ∼120 km) the drifts are largely uniform with altitude (latitude) and represent the fact that the flow is predominantly zonal, that the plasma is collisionless, and that the ions are $\mathbf{E} \times \mathbf{B}$ drifting. The collisional coupling between the ions and neutral means that the ions will transition from flowing perpendicular to applied forces (i.e., $\mathbf{E} \times \mathbf{B}$ drifting) to flowing parallel to the applied forces (i.e., with the neutral wind) with decreasing altitude [e.g., *Tsunoda et al.*, 2007]. At intermediate altitudes ($\kappa_i \sim 1$), the ions will drift ∼45° to the applied forces. At lower altitudes, one sees the drifts change dramatically, with a "band" of enhanced meridional flow centered at about 115 km, with the altitude decreasing with time. This feature must be induced by a meridional wind and the downward progression caused by tidal/large-scale wave behavior. This will be shown and discussed shortly when the neutral winds are presented.

[33] The derived vector velocities for this night are shown in Figure 6. The data here were processed at about two-minute time resolution. To compute the drift estimates in Figure 6 (top, colored), the two-minute data were binned into 0.5° magnetic latitude bins every 0.25°. As expected, the errors on the drift estimates increase farther down range, since (1) signal to noise ratios are decreasing and (2) fewer measurements are going into each individual resolved vector. In addition, the beams are becoming farther apart, so the assumption of zonal spatial uniformity could be breaking down. The large errors in the lowest latitudinal bin are the result of few measurements in this bin that satisfy the minimum altitude criteria. In this case, the solution is being driven by the a priori information. For the a priori matrix, we have assumed diagonality and chosen standard errors of 3000 m/s for the perpendicular directions and 15 m/s for the parallel direction. The parallel number was chosen by examining the statistics of a long duration data set of up-
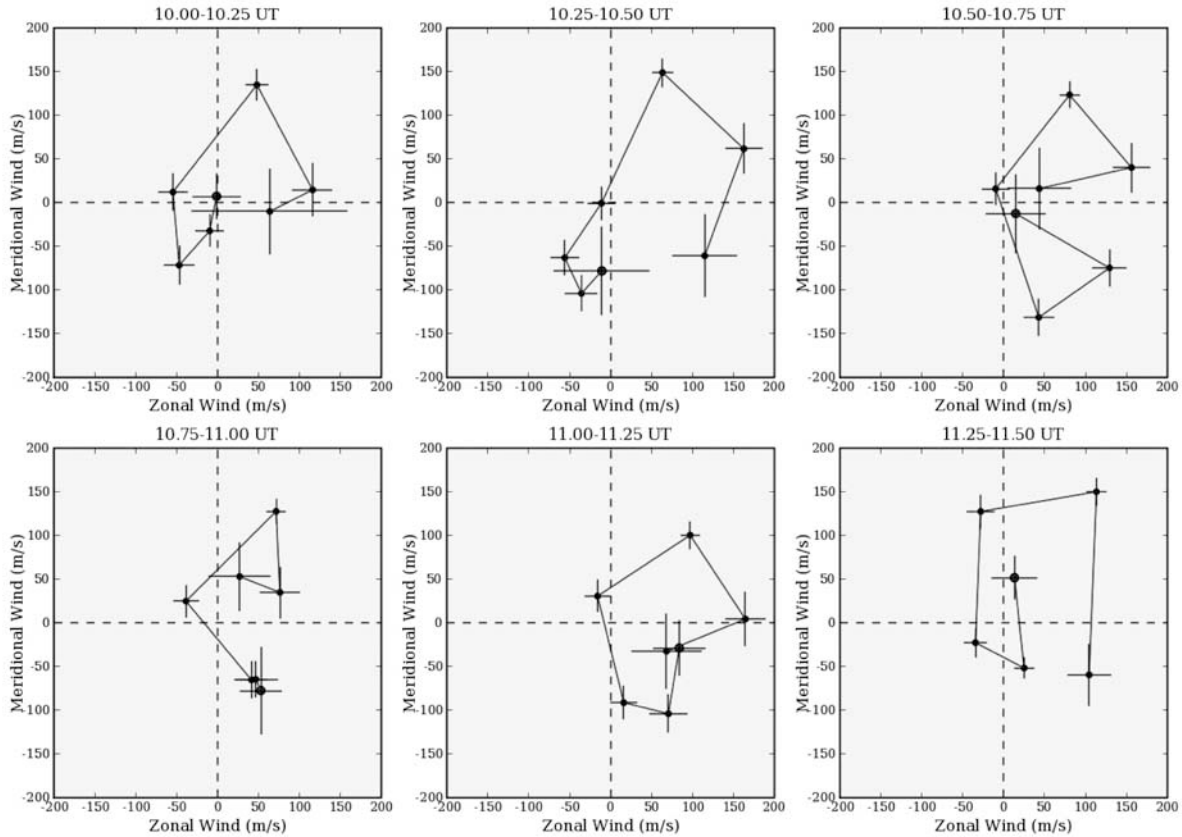
Figure 8. Hodographs of the *E*-region winds for the same time period as Figure 7 with errorbars indicated. The blue dot corresponds to the lowest altitude bin (90–95 km).

B measurements. The parallel errors frequently relax to the a priori value (15 m/s).

[34] In the top quiver plot, the data have been integrated for 10 minutes for display purposes (that is five 2-minute estimates were passed to the inversion routine, with each measurement being considered an independent estimate of the velocity field within that time interval). Prior to magnetic midnight (which occurs just after 11 UT), the drifts are predominantly westward (magnitude near 500–1000 m/s) with a weak northward component (about 100 m/s). After the reversal, the drifts transition to eastward and the meridional component (eastward electric field) also reverses. There is also a clear latitudinal gradient showing stronger drifts at higher latitudes. Close to magnetic midnight, the drifts decrease over a period of 1–2 hours before reversal. The bottom plot shows a zoomed-in quiver plot, where we now expand the time resolution to 2 minutes. Here we can clearly see the structure of the reversal drifts, which show strong latitudinal gradients. The power of the approach is evident in the latitudinal channel of westward drifts embedded in

the reversal region at about 10:47 UT, which is seen in the top color plots and the lower 2-minute quiver plot, but not in the 10-minute quiver plot. After the reversal, the eastward component of the drift increases very rapidly, exceeding 1000 m/s with a strong latitudinal gradient. In this case, PFISR is likely probing the edge of the convection boundary. Enhanced precipitation after local magnetic midnight is a feature observed frequently in PFISR data and is indicative of PFISR moving from a subauroral location into the auroral oval.

[35] Turning to the neutral winds on this night, Figure 7 shows profiles of zonal and meridional winds processed using the scheme developed in section 3.4. These data have been processed with 2-minute long pulse data and 5-minute alternating code data, with measurements combined into 5-km altitudinal bins. The wind profiles were subsequently integrated for 15 minutes. In this analysis, the pair of beams farthest downrange was neglected because of the significant latitudinal gradient in electric field that was apparent in Figure 6. The winds were also cutoff at the altitude where the relative errors become

large, which results from the transition of a collisional to collisionless plasma. The wind results are consistent from one profile to the next and show trends expected at these altitudes. The winds are wavelike in altitude and show a shear region with a maximum near $110-115$ km for the meridional wind and slightly higher for the zonal wind. The band of enhanced meridional winds that was postulated from inspection of the line-of-sight velocities in Figure 5 is evident. The peak values are close to 100 m/s in both the meridional and zonal directions. These values are within the range expected as reported by *Larsen* [2002] based on decades of chemical release measurements. Figure 8 shows hodographs for these same profiles, which are useful for evaluating the vertical shear in the horizontal wind. The rotation of the flow with altitude and the maximum wind in the meridional direction near $110-115$ km is clear.

5. Conclusion

[36] In this paper, we have presented the technique used to resolve vector velocities with the PFISR from an arbitrary set of vector velocities based on casting the problem into a Bayesian linear model form. The approach is also applicable to any other AMISR system, and can also be adapted to scanning systems such as Sondrestrom, Millstone Hill, or Arecibo. The method is ideally suited for the AMISR systems where the problem is in general overdetermined. It is also straightforward to plan an appropriate set of look directions for a given scientific study with the method since the output covariance matrix of the approach is independent of the magnitude of the measured drifts. We have also extended the method to the estimation of *E*-region neutral winds and made use of the approach's a priori covariance to combine priors appropriate for *F* region electric field measurements, where it can be assumed that the parallel electric field is negligible, with priors appropriate to wind estimates, where it can be assumed that the vertical wind is negligible. This approach has numerous other applications, in particular to steering systems where temporal/spatial ambiguity can be partially compensated for by utilizing continuous representations of expected temporal/spatial variations subject to appropriate a priori specifications.

References

Aster, R. C., B. Borchers, and C. H. Thurber (2005), *Parameter Estimation and Inverse Problems*, Elsevier Acad. Press, San Diego, CA.

Azeem, S. M. I., and R. M. Johnson (1997), Lower thermospheric neutral winds at Sondre Stromfjord: A seasonal analysis, *J. Geophys. Res.*, *102*(A4), 7379–7397.

Banks, P. M., J. C. Foster, and J. R. Doupnik (1981), Chatanika radar observations relating to the latitudinal and local time variations of Joule heating, *J. Geophys. Res.*, *86*(A8), 6869–6878.

Brekke, A., and J. R. Doupnik (1973), A preliminary study of the neutral wind in the auroral E region, *J. Geophys. Res.*, *78*(34), 8235–8250.

de la Beaujardière, O., R. Vondrak, and M. Baron (1977), Radar observations of electric fields and currents associated with auroral arcs, *J. Geophys. Res.*, *82*(32), 5051–5062.

Doupnik, J. R., P. M. Banks, M. J. Baron, C. L. Rino, and J. Petriceks (1972), Direct measurements of plasma drift velocities at high magnetic latitudes, *J. Geophys. Res.*, *77*(22), 4,268–4,271.

Evans, J., J. Holt, and R. Wand (1979), Millstone Hill incoherent scatter observations of auroral convection over $60° \leq \Lambda \leq 75°$, 1. Observing and data reduction procedures, *J. Geophys. Res.*, *84*(A12), 7059–7074.

Evans, J., J. Holt, W. Oliver, and R. Wand (1980), Millstone Hill incoherent scatter observations of auroral convection over$° \leq \Lambda \leq 75°$, 2. Initial results, *J. Geophys. Res.*, *85*(A1), 41–54.

Fedder, J. A., and P. M. Banks (1972), Convection electric fields and polar thermospheric winds, *J. Geophys. Res.*, *77*(13), 2328–2340.

Foster, J. C., J. R. Doupnik, and G. S. Stiles (1981), Large scale patterns of auroral ionospheric convection observed with the Chatanika radar, *J. Geophys. Res.*, *86*(A13), 11,357–11,371.

Hagfors, T., and R. A. Behnke (1974), Measurements of three-dimensional plasma velocities at Arecibo, *Radio Sci.*, *92*(A4), 3345–3355.

Hedin, A. E. (1991), Extension of the MSIS thermosphere model into the middle and lower atmosphere, *J. Geophys. Res.*, *96*(A2), 1159–1172.

Holt, J. M., and A. P. van Eyken (2000), Plasma convection at high latitudes using the EISCAT VHF and ESR incoherent scatter radars, *Ann. Geophys.*, *18*, 1088–1096.

Holt, J. M., J. V. Evans, W. L. Oliver, and R. H. Wand (1984), Millstone Hill observations of ionospheric convection, in *Proceedings of the 1982-4 MIT Symposia*, pp. 53–72, Scientific Publishers, Inc.

Holt, J. M., R. H. Wand, J. V. Evans, and W. L. Oliver (1987), Empirical models for the plasma convection at high latitudes from Millstone Hill observations, *J. Geophys. Res.*, *92*(A1), 203–212.

Horwitz, J., J. Doupnik, and P. Banks (1978), Chatanika radar observations of the latitudinal distributions of auroral zone

electric fields, conductivities, and currents, *J. Geophys. Res.*, *83*(A4), 1463–1481.

Hysell, D. L. (2007), Inverting ionospheric radio occultation measurements using maximum entropy, *Radio Sci.*, *42*, RS4022, doi:10.1029/2007RS003635.

Hysell, D. L., G. Michhue, M. F. Larsen, R. Pfaff, M. Nicolls, C. Heinselman, and H. Bahcivan (2008), Imaging radar observations of Farley Buneman waves during the JOULE II experiment, *Ann. Geophys.*, *26*, 1837–1850.

Johnson, R. M. (1990), Lower-thermospheric neutral winds at high latitude determined from incoherent scatter measurements: A review of techniques and observations, *Adv. Space Res.*, *10*(6), 261–275.

Johnson, R. M., and T. S. Virdi (1991), High-latitude lower thermospheric neutral winds at EISCAT and Sondrestrom during LTCS 1, *J. Geophys. Res.*, *96*(A2), 1099–1116.

Johnson, R. M., V. B. Wickwar, R. G. Roble, and J. G. Luhmann (1987), Lower-thermospheric winds at high latitude: Chatanika radar observations, *Ann. Geophys.*, *5A*(6), 383–404.

Kelley, M. C. (1989), *The Earth's Ionosphere: Plasma Physics and Electrodynamics*, Academic Press, San Diego, Calif.

Larsen, M. F. (2002), Winds and shears in the mesosphere and lower thermosphere: Results from four decades of chemical release wind measurements, *J. Geophys. Res.*, *107*(A8), 1215, doi:10.1029/2001JA000218.

Lehtinen, M. S., and I. Häggström (1987), A new modulation principle for incoherent scatter measurements, *Radio Sci.*, *22*(4), 625–634.

Nicolls, M. J., and C. J. Heinselman (2007), Three-dimensional measurements of traveling ionospheric disturbances with the Poker Flat Incoherent Scatter Radar, *Geophys. Res. Lett.*, *34*, L21104, doi:10.1029/2007GL031506.

Nicolls, M. J., C. J. Heinselman, E. A. Hope, S. Ranjan, M. C. Kelley, and J. D. Kelly (2007), Imaging of polar mesosphere summer echoes with the 450 MHz poker flat advanced modular incoherent scatter radar, *Geophys. Res. Lett.*, *34*, L20102, doi:10.1029/2007GL031476.

Pfaff, R. F. (1996), In-situ measurement techniques for ionospheric research, in *Modern Ionospheric Science*, edited by H. Kohl, R. Rüster, and K. Schlegel pp. 459–551, Eur. Geophys. Soc., Katlenburg-Lindau, Germany.

Richmond, A. D. (1995), Ionospheric electrodynamics using magnetic apex coordinates, *J. Geomagn. Geoelectr.*, *47*(2), 191–212.

Schlegel, K., and D. R. Moorcroft (1989), EISCAT as a tristatic auroral radar, *J. Geophys. Res.*, *94*(A2), 1430–1438.

Sulzer, M. P., N. Aponte, and S. A. González (2005), Application of linear regularization methods to Arecibo vector velocities, *J. Geophys. Res.*, *110*, A10305, doi:10.1029/2005JA011042.

Tarantola, A. (2005), *Inverse Problem Theory and Methods for Model Parameter Estimation*, Soc. for Ind. and App. Math., Philadelphia, PA.

Thayer, J. P. (1998), Height-resolved Joule heating rates in the high-latitude E region and the influence of neutral winds, *J. Geophys. Res.*, *103*(A1), 471–487.

Thayer, J. P. (2000), High-latitude currents and their energy exchange with the ionosphere-thermosphere system, *J. Geophys. Res.*, *105*(A10), 23,015–23,024.

Tsunoda, R. T., P. Stauning, and J. K. Olesen (2007), On electrodynamical measurements in the polar ionosphere with a monostatic incoherent scatter radar, *Radio Sci.*, *42*, RS2013, doi:10.1029/2006RS003471.

Vadas, S. L., and M. J. Nicolls (2008), Using PFISR measurements and gravity wave dissipative theory to determine the neutral thermospheric winds, *Geophys. Res. Lett.*, *35*, L02105, doi:10.1029/2007GL031522.

VanZandt, T. E., W. L. Clark, and J. M. Warnock (1972), Magnetic apex coordinates: A magnetic coordinate system for the ionospheric F2 layer, *J. Geophys. Res.*, *77*(13), 2406–2411.

Wand, R. H., and J. V. Evans (1981), Seasonal and magnetic activity variations of ionospheric electric fields over millstone hill, *J. Geophys. Res.*, *86*(A1), 103–118.

Williams, P. J. S., G. O. L. Jones, and A. R. Jain (1984), Methods of measuring plasma velocity with EISCAT, *J. Atmos. Terr. Phys.*, *46*, 521–530.

C. J. Heinselman and M. J. Nicolls, Center for Geospace Studies, SRI International, 333 Ravenswood Avenue, Menlo Park, CA 94025, USA. (craig.heinselman@sri.com; michael.nicolls@sri.com)